Effect of temperature on the activities and stabilities of hydrothermally prepared IrO$_x$ nanocatalyst layers for the oxygen evolution reaction

Gabriel C. da Silva, Nickson Perini, Edson A. Ticianelli[*]

Instituto de Química de São Carlos, USP, C.P 780, São Carlos, SP 13560-970, Brazil

ABSTRACT

Iridium oxide nanoparticles are prepared via a hydrothermal method, treated at different calcination temperatures, and their activities and stabilities for the oxygen evolution reaction (OER) evaluated. The catalysts are physicochemically characterized using several techniques including X-ray diffraction, energy dispersive X-ray spectroscopy, transmission electron microscopy, X-ray photoelectron spectroscopy, and X-ray absorption spectroscopy. Voltammetric profiles obtained for the catalysts calcined up to 300 °C are similar to that of electrochemically prepared hydrous iridium oxide, while the CV profiles are characteristic of thermally prepared iridium oxide after calcination at higher temperatures. Performance as an OER catalyst decreases with increasing IrO$_x$ calcination temperature, while the opposite trend in stability is observed for these materials. Catalysts calcined between 400 and 500 °C exhibit better balances between activity and stability. However, despite higher performance losses, the non-calcined IrO$_x$ material still exhibits higher mass activity at the end of the aging experiments at electrode potentials up to 1.6 V vs. RHE. The causes of electrode activity degradation are investigated using identical location transmission electron microscopy, which reveal that IrO$_x$ electrode instability is due to the degradation of the thin IrO$_x$ layer, in addition to iridium oxide dissolution.

© 2017 Elsevier B.V. All rights reserved.

1. Introduction

The dependency on traditional fossil fuels, together with environmental problems caused by their production and consumption, has incentivized the development of alternative energy conversion devices that use clean and renewable fuels. A promising alternative to an economy based on fossil fuels is one based on hydrogen, a nonpolluting fuel that can be used in fuel cells with higher energy conversion efficiencies compared to internal combustion engines [1,2]. A clean way of obtaining hydrogen fuel is through the electrolysis of water using a proton exchange membrane water electrolyzer (PEMWE) in a process that splits water into hydrogen (H$_2$) and oxygen (O$_2$) through the cathodic hydrogen evolution reaction (HER) and the anodic oxygen evolution reaction (OER), respectively [3,4]. At the cathode, HER takes place with low overpotential values when platinum is used as the electrocatalyst [5,6]. In contrast, the OER involves a much more complex mechanism, resulting in slow kinetics and high electrode overpotentials [7,8].

Ruthenium- and iridium-based catalysts are conventional choices for PEMWE anodes. Cherevko et al.[9] compared the activities of sputtered Ru and Ir films, and also of the oxidized RuO$_2$ and IrO$_2$ films. Both unoxidized metals were more active than their respective oxides, however metal dissolution was 2–3 orders of magnitude higher compared to the oxides. In addition, IrO$_2$ was more stable than RuO$_2$, with a metal-dissolution rate 30 times smaller than that of RuO$_2$. The higher stability of IrO$_2$ has also been reported in other papers, justifying the choice of iridium oxide as an OER catalyst in acidic media [10–14]. However, despite the good activity and superior stability of IrO$_2$, iridium is a scarce and expensive metal; therefore its use should be optimized in order to reduce PEMWE prices.

Generally, iridium oxide is obtained electrochemically by the anodic oxidation of metallic iridium, through the thermal decomposition of an iridium precursor, or chemically, usually by the Adams fusion method. Some studies have shown that changing the structural properties of IrO$_2$ is a satisfactory way of improving the activity and the stability of the electrocatalyst. Regarding the activity for the OER, usually amorphous iridium oxide is regarded to be more active than the crystalline version, while the latter is considered to be more stable. Ouattara et al. [15] compared the OER activity of an amorphous IrO$_2$ film prepared by the anodic oxida-

* Corresponding author.
  E-mail address: edsont@iqsc.usp.br (E.A. Ticianelli).

tion of metallic iridium, also referred to as a "hydrous iridium oxide film", with that of a crystalline film prepared by the thermal decomposition of an iridium precursor. Both the specific electrocatalytic activity and Tafel slope for the OER in these films were similar, but no stability comparison studies were performed.

Reier et al. [16] investigated the OER performance of IrO_2 thin films prepared by the thermal decomposition of iridium acetate at various calcination temperatures. The electrocatalytic activities of the films prepared at 250 and 350 °C were almost identical, but superior compared to films calcined at 450 and 550 °C. The better performance of the former films was attributed to the presence of a mixture of amorphous and crystalline IrO_2. In another study, the authors used on-line ICP-MS experiments to reveal that both calcination temperature and the crystallinity of the IrO_2 film affect the Ir dissolution rate, with the stability essentially increasing with increasing calcination temperature [17].

An easy way obtaining iridium oxide nanoparticles with different structural proprieties was demonstrated by Bestaoui and Prouzet [18]; these authors prepared a chloride-free amorphous iridium oxide by the slow hydrolysis of $IrCl_3$ followed by autoclave treatment. Posterior material calcination revealed that the oxide began to crystallize into the IrO_2 rutile structure above 450 °C, however no electrochemical experiments were performed. Here, we synthesized IrO_x electrocatalysts with a variety of structural proprieties using the hydrothermal method previously described [18]. The catalysts were characterized using several techniques such as thermogravimetric analysis, specific surface area (BET theory) analysis, energy dispersive X-ray spectroscopy, X-ray diffraction, X-ray photoelectron spectroscopy, transmission electron microscopy, and X-ray absorption spectroscopy. The prepared materials were electrochemical characterized and their OER activities evaluated in half-cell configurations in an acidic electrolyte, while the stabilities of the materials were evaluated using two stability protocols. To better understand the stability of each catalyst, identical location transmission electron microscopy (ILTEM) experiments were performed, which, to our knowledge, has not previously been used to study IrO_2 during the oxygen evolution reaction.

2. Experimental section

2.1. Catalysts synthesis

Iridium oxide catalysts with varying degrees of crystallinity were synthesized according to hydrothermal method of Bestaoui and Prouzet [18]. A solution of the iridium precursor was prepared by dissolving 5 g of $H_2IrCl_6 \cdot xH_2O$ (99 wt%, Alfa Aesar) in 100 mL of ultrapure water (18.2 MΩ cm, Milli-Q). A 1 M solution of LiOH (99 wt%, Sigma-Aldrich) was added by syringe pump to 10 mL of the prepared solution at a rate of 0.2 mL h^{-1} until the molar ratio of [OH$^-$] to [Cl$^-$] was six. Ultrapure water was then added to achieve a final volume of 50 mL, after which the solution was transferred to a Teflon bottle which was placed in an autoclave compartment at 180 °C for 24 h.

After autoclaving, the black precipitate that formed was separated from the colorless supernatant, collected with a 0.2 μm PTFE filter and washed with boiling water. The IrO_x catalyst was finally dried at 50 °C for 1 h. The catalyst prepared in this manner is referred to as "aut-IrO_x". In order to obtain different degrees of crystallinity, aut-IrO_x was subjected to temperatures that ranged from 100 to 500 °C in air for 1 h.

2.2. Physicochemical characterization

The thermal stability of each IrO_x catalyst was evaluated by thermogravimetric analysis (TGA) using a Metler-Toledo TGA/DSC 2 STARe system at an air flow rate of 50 mL min^{-1} and a temperature ramp of 10 °C min^{-1}. The masses and atomic compositions of the materials were determined using energy dispersive X-ray spectroscopy (EDX) using a Leica-Zeiss LEO 440 scanning electron microscope at an accelerating voltage of 40 kV. The crystalline structures of the synthesized electrocatalysts were analyzed by X-ray diffraction (XRD) using a Bruker D8 Advance diffractometer with KαCu radiation (1.5406 Å); the data were collected for 2θ values between 10 and 100° at a rate of 0.075° s^{-1}.

The specific surface areas and pore volumes of the catalysts were determined using a Quantachrome NOVA-1000 instrument. The specific surface area was evaluated using the Brunauer-Emmett-Teller (BET) method. The catalyst samples were degassed at 373 K for 3 h before obtaining isotherms at 77 K. Transmission electron microscopy (TEM) was performed with a JEOL JEM-2100 instrument fitted with a LaB$_6$ filament at an accelerating voltage of 200 kV. Sample grids were prepared by dispersing the electrocatalysts in isopropanol and depositing single drops on carbon-film copper grids (EMS, 400 mesh).

The chemical environments and the surface compositions of the electrocatalysts were evaluated by X-ray photoelectron spectroscopy (XPS). The spectra were acquired at the Laboratório Nacional de Nanotecnologia (LNNano, Campinas – Brasil) on a Thermo Scientific K-Alpha+ spectrometer using 1487 eV X-rays and an aluminum monochromator. The binding energies were calibrated with respect to the C 1s energy at 284.8 eV. In-situ X-ray absorption spectroscopy (XAS) experiments were conducted in transmission mode. A catalyst pellet composed of 10 mg$_{Ir}$ cm^{-2} mixed with 10 wt% Nafion deposited from a solution containing 6 wt% Nafion in low-aliphatic alcohols (DuPont) was used as the working electrode. XAS data were collected using a reversible hydrogen electrode (RHE) and a Pt screen as reference and counter electrode, respectively, in 0.5 M H_2SO_4 as the electrolyte. XAS measurements were performed at the Laboratório Nacional de Luz Sincrotron (LNLS, Campinas – Brasil) and the spectra were collected at the Ir L$_3$ edge at 0.2, 1.0, 1.45 and 1.6 V. Data processing was conducted using the ATHENA XAS data processing software [19].

2.3. Electrochemical experiments

Electrochemical experiments were performed using a standard three-electrode electrochemical cell, in argon-purged 0.5 M H_2SO_4 electrolyte at 25 °C, using a Solartron 1285 potentiostat. RHE and platinum foil were used as reference and counter electrode, respectively, while the working electrode substrate was a glassy carbon disc (0.196 cm^2) inserted into a Teflon sleeve, polished to a mirror surface. The working electrode consisted of a catalyst layer containing 0.38 mg$_{Ir}$ cm^{-2}. This layer was prepared by dispersing 5 mg of the catalyst powder and 30 μL of Nafion solution (6 wt%, DuPont) in 1 mL of isopropanol, which was deposited onto the carbon substrate using a micropipette.

Initially, the prepared IrO_x catalysts were characterized by cyclic voltammetry (CV) between 0.05 and 1.2 V at different sweep rates. The electrochemically active surface areas (ECSAs) were assumed to be proportional to the anodic redox charge of the CVs, as proposed by Ardizone et al. [20]. Here the results were obtained by integration of the anodic voltammetric profiles at various sweep rates.

The OER activities of the catalysts were evaluated by potential cycling between 1.1 and 1.6 V at 5 mV s^{-1}. To avoid the accumulation of oxygen bubbles, a rotation speed of 1600 rpm was applied using a Pine rotator system. The catalysts' stabilities were examined using two protocols: (i) 1000 potential cycles between 0.3 and 1.2 V at 50 mV s^{-1}, which has already been used in stability studies of OER catalysts [21], and (ii) 500 potential cycles between 1.1 and 1.6 V
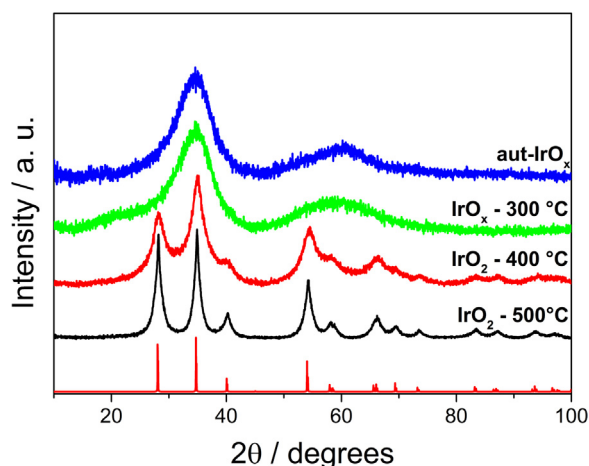
Fig. 1. XRD patterns for the aut-IrO$_x$ catalyst and for the oxides treated at 300, 400 and 500 °C. Vertical lines correspond to the tetragonal IrO$_2$-rutile crystallographic structure pattern (JCPDS No. 15-870).

at 50 mV s^{-1}, which covers the OER potential window. Chronoamperometry experiments were carried out for 1 h at 1.55 V in order to follow the evolution of the electrodes' activities as functions of time.

Electrochemical impedance spectroscopy (EIS) experiments were conducted using an Autolab PGSTAT30 potentiostat/galvanostat equipped with a frequency response analyzer (FRA). EIS spectra were acquired potentiostatically under open circuit conditions after a conditioning period of 2 min. A perturbation amplitude of 10 mV over the 100 kHz to 0.1 Hz frequency range was employed.

2.4. Identical location transmission electron microscopy (ILTEM) experiments

ILTEM experiments were carried out using same TEM instrumentation described in part 2.2 above. However, for these experiments a single drop of the catalyst ink (prepared for the electrochemical studies) was deposited on a Lacey carbon gold grid (EMS, 300 mesh). Initial TEM images of the catalysts were collected at different regions. The catalysts were then aged over 500 potential cycles between 1.1 and 1.6 V at 50 mV s^{-1} using the TEM grid as the working electrode. Final images were collected at the same regions previously chosen to evaluate the effects of electrochemical aging on the catalysts.

3. Results and discussion

3.1. Compositional and structural characterization of the catalysts

Detailed descriptions of the synthesis routes used to prepare the IrO$_x$ catalyst, and the material obtained after the autoclave treatment process (aut-IrO$_x$) are provided in the Supplementary Information. In order to determine the different degrees of crystallinity, the aut-IrO$_x$ catalyst was submitted to heat treatment in the 100–500 °C temperature range. As presented in the Supplementary Information, the EDX results reveal that iridium and oxygen are the predominant elements in the synthesized catalysts, and that heat treatment leads to slight increases in the iridium content at the detriment of oxygen.

Fig. 1 displays the XRD profiles of the aut-IrO$_x$ catalyst and the materials obtained after calcination at 300, 400, and 500 °C (referred to as "IrO$_x$ – 300 °C", etc.). The XRD profiles of the IrO$_x$

– 100 °C and IrO$_x$ – 200 °C catalysts are similar to those obtained for aut-IrO$_x$ and IrO$_x$ – 300 °C and are therefore not shown. As is evident from the XRD profiles, the catalyst obtained after autoclaving and the one submitted to heat treatment at 300 °C have similar XRD profiles. Two large peaks are clearly visible in both XRD patterns; these peaks are attributable to the most intense peaks of the rutile and hollandite phases of IrO$_2$ [22–24]. The XRD results for these catalysts are characteristic of materials that are amorphous and/or have small-sized crystallites.

By increasing the calcination temperature to 400 °C, the amorphicity of the electrocatalyst was observed to decrease. In addition, peaks related to reflections from the tetragonal rutile IrO$_2$ crystallographic structure can easily be distinguished (vertical lines). After raising the temperature to 500 °C, these reflection peaks became thinner and sharper, indicating a higher degree of crystallinity for this material; the XRD pattern also confirmed the absence of other phases such metallic iridium. These materials are referred to as "IrO$_2$ – 400 °C" and "IrO$_2$ – 500 °C".

The structural parameters for each IrO$_2$ electrocatalyst, such as mean crystallite size and the lattice parameter, were evaluated through Rietveld refinement [25]. The mean crystallite size determined for IrO$_2$ – 400 °C is 3.4 nm, while that for the material obtained at 500 °C is 13.7 nm. For the amorphous catalysts, the absence of defined diffraction peaks makes it impossible to use the Rietveld method, which meant that the mean crystallite sizes of the materials treated at temperatures at or below 300 °C could not be determined. The lattice parameters for the IrO$_2$-based catalysts were determined to be: a = 4.4895 Å and c = 3.1450 Å for IrO$_2$ – 400 °C, and a = 4.4983 Å and c = 3.1450 Å for the IrO$_2$ – 500 °C material (see Table S1), which are in accordance with the JCPDS database (JCPDS No. 15-870).

Transmission electron micrographs for the aut-IrO$_x$, IrO$_x$ – 300 °C, IrO$_2$ – 400 °C, and IrO$_2$ – 500 °C catalysts are presented in Fig. 2. The presence of aggregates composed of small particles, which are characteristic of unsupported catalysts, are observed in all images. The TEM micrograph of the aut-IrO$_x$ catalyst reveals spherical particles with sizes in the 1–2 nm range, but the mean particle size could not be determined due to the agglomeration of these nanoparticles. Similar profiles were observed for the IrO$_x$ – 100 °C and 200 °C materials shown in Figs. S1a and S1b . For the catalysts obtained at 300, 400 and 500 °C (Fig. 2b–d) spherical morphologies are no longer evident. Furthermore, the particle sizes increase due to coalescence resulting as a consequence of the thermal treatment. Some boundary zones observed for the IrO$_2$ – 500 °C catalyst are evidence of the majority presence of particles with sizes in the 10–15 nm range, in agreement with the XRD results (Table S1).

Fig. 3 displays the high resolution XPS spectra of the Ir 4f orbital of all electrocatalysts. Each Ir 4f spectrum can be deconvoluted into two sets of doublets, which can be assigned to iridium in different oxidation states; the less intense doublet, with 7/2 and 5/2 spin-orbit components located at 61.8 and 64.7 eV, respectively, corresponds to Ir^{3+}, while the main doublet, with components located at 62.8 and 65.6 eV is attributed to Ir^{4+}. These energy values are consistent with other results reported in the literature and confirm the absence of metallic iridium (Ir^0), in agreement with in the XRD data [26–28]. Each spectrum also exhibits a satellite peak due to conduction-band interactions during photoemission [26]. Table 1 summarizes the binding energies of the Ir 4f$_{7/2}$ orbitals, as well as the percentage contribution of each oxidation state of the studied materials. All synthesized catalysts contain Ir^{4+} as the predominant species ($\sim$70%). However, the Ir^{3+} content was observed to increase slightly with increasing calcination temperature, but remained close to approximately one third of the atomic composition of each electrocatalyst.

High-resolution oxygen 1s-orbital spectra were also acquired and are displayed in Fig. S2. For simplification, only spectra for aut-
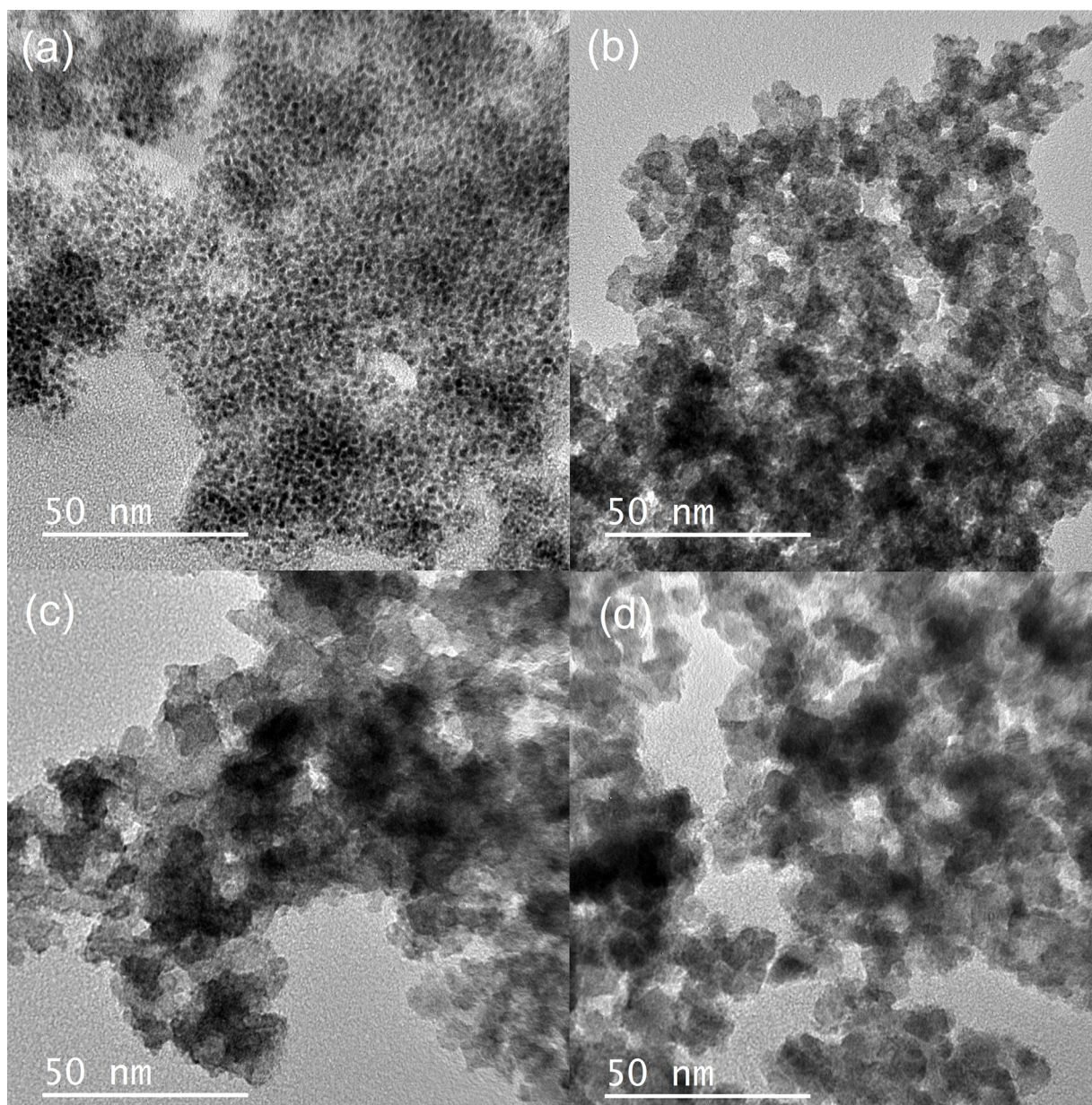
Fig. 2. TEM images of the electrocatalysts: (a) aut-IrO_x, (b) IrO_x – 300 °C, (c) IrO_2 – 400 °C, and (d) IrO_2 – 500 °C.
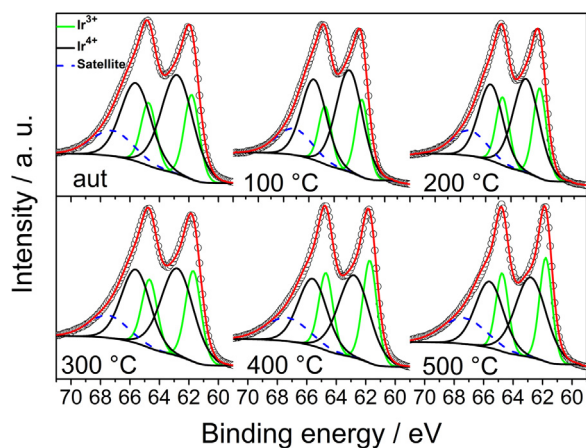

Fig. 3. High resolution XPS spectra corresponding to the Ir 4f orbitals of the IrO_x electrocatalysts.

Table 1
The binding energy (B. E.) of each Ir $4f_{7/2}$ component and the atomic percentage of Ir^{3+} and Ir^{4+} in each studied electrocatalyst.

IrO_x	Ir^{3+}		Ir^{4+}	
	B. E. (eV)	Atomic percentage	B. E. (eV)	Atomic percentage
aut	61.8	29	62.8	71
100 °C	61.8	27	62.8	73
200 °C	61.7	33	62.8	67
300 °C	61.7	33	62.8	67
400 °C	61.7	36	62.8	64
500 °C	61.8	35	62.8	65

IrO_x, IrO_x – 300 °C and IrO_2 – 500 °C are shown. These spectra reveal that the O1s orbital shifts to lower energy with increasing calcination temperature. This shift reflects an enhancement in the oxygen content of the oxide form compared to the oxy-hydroxide [29,30]. In addition, as detailed in the Supplementary Information, the ratios of the XPS signal intensities, I_O/I_{Ir}, clearly demonstrate that some
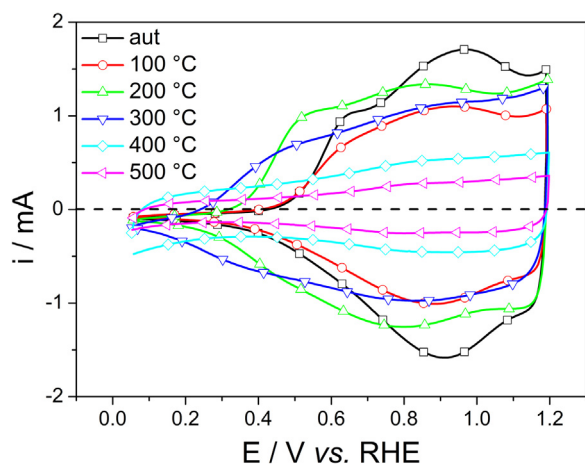
Fig. 4. Cyclic voltammograms of IrO_x prepared at different temperatures at a scan rate of $50 \, mV \, s^{-1}$ in $0.5 \, M \, H_2SO_4$ at $25 \, °C$.

Table 2
BET surface area (S), pore volume (V_p), and total CV charge (Q_{Total}) obtained for each IrO_x electrocatalysts.

IrO_x	S ($m^2 \, g^{-1}$)	V_p ($cm^3 \, g^{-1}$)	Q_{Total} ($mC \, cm^{-2}$)
aut	141	0.291	95
100 °C	131	0.265	67
200 °C	108	0.237	96
300 °C	75	0.165	92
400 °C	55	0.145	38
500 °C	10	0,106	20

loss of oxygen at the catalysts surface is associated with the conversion of Ir^{4+} into Ir^{3+}, as confirmed by the results in Table 1, and/or by the release of some water of hydration (see TGA result in Fig. S3).

Since XPS is a surface-sensitive technique, the atomic percentages of the Ir (III) and Ir (IV) components presented in Table S2 are more accurate for aut-IrO_x and the materials treated up to 200 °C, because of their smaller particle sizes; for the materials with larger particle sizes, the bulk compositions may be somewhat different of those indicated by XPS because the XPS results do not provide the overall proprieties of these materials. Despite this, the XPS data in Table 1 are in agreement with the observed lower oxygen content of materials heat treated at the higher temperatures, as observed by EDX (Table S1).

3.2. Surface electrochemistry and electronic properties

Fig. 4 depicts the cyclic voltammograms (CVs) of the studied IrO_x electrocatalysts. The CV profiles of the aut-IrO_x and IrO_x – 100 °C materials display irreversible pre-peaks at ~0.6 V, which are linked to the insertion of HSO_4^-/SO_4^{2-} anions from the electrolyte solution [31], followed by reversible peaks at 0.9 V that correspond to the Ir(III)/Ir(IV) redox couple. These profiles are similar to that reported in the literature for electrochemically prepared iridium oxide [15,32]. For the materials prepared at 200 and 300 °C, the first CV peak shifts to lower potential and, moreover, the Ir(III)/Ir(IV) redox peak gradually becomes less evident with increasing temperature. After annealing at temperatures of 400 and 500 °C, the CVs exhibit capacitive profiles similar to that of iridium oxide obtained by the direct thermal decomposition of iridium precursors [15,33].

The growth and coalescence of particles, as seen by TEM and ILTEM (see below) provide an explanation for the differences observed in the cyclic voltammogram of the studied IrO_x electrocatalysts. Despite increases in the Ir^{3+}/Ir^{4+} ratio with increasing treatment temperature (Table 1), the voltammetric charge of the redox peak decreases, because of decreases in the exposed surface area and the anion insertion difficulties inside the IrO_x structure, particularly at temperatures in excess of 400 °C.

The oxidation states of the Ir-oxide catalysts at several electrode potentials were further investigated using in-situ X-ray absorption spectroscopy (XAS). The XANES regions of the spectra of the aut-IrO_x and IrO_2 – 500 °C catalysts are presented in Fig. 5 at several electrode potentials. For aut-IrO_x, data could not be collected at 1600 mV due to the formation of oxygen bubbles. The peaks observed in the XANES spectra result from Ir 2p to 5d orbital electronic transitions. For both samples, as the applied potential is

increased, the Ir L_3 edge shifts to higher energy values, as evidenced by shifts in the XANES peak positions. This behavior has been reported previously and is assigned to changes in the Ir distribution across the Ir^{+3} and Ir^{+4} oxidation states in the catalysts [34,35]. For aut-IrO_x this shift is more intense, which is evidence of greater oxidation of Ir^{3+} to Ir^{4+}, or even to higher oxidation states, as the potential approaches the OER onset. The occurrence of such a process is clearly evidenced by the CV results presented in Fig. 4. In addition, since electrochemical oxidation takes place only at particle surfaces, changes in the XANES signals are more pronounced for smaller particles, in agreement with the present results. A shift in the Ir L_3 edge to higher energy with increasing electrode potential is also observed for the IrO_2 – 500 °C catalyst, but this is much less pronounced compared to that observed for aut-IrO_x, in agreement with the smaller redox currents seen in the CV (Fig. 4). Abbott et al.[36] compared the XANES spectra of IrO_2 after calcination at 350 and 600 °C. No shift in the edge energy was observed with increasing electrode potential for the sample treated at higher temperature, indicating that there was no measurable change in the iridium oxidation state, as is also observed here.

In addition to the observed changes in edge energy, the Ir L_3 peak intensity, also known as the white line intensity, decreased slightly, particularly for aut-IrO_x, as the electrode potential was increased to more anodic values. Increases in the white line intensities have been widely reported for Pt-based electrocatalysts and are due to changes in the Pt d-band as a result of the withdrawal of electrons from the 5d-band during the formation of oxo species [37–40]; a similar trend was reported for IrO_2 [34,41]. Abbott et al.[36] observed a similar trend for IrO_2 calcined at 350 and 600 °C and associated the decrease in the Ir L_3 edge intensity to changes in the Ir 5d-states as the electrode is polarized. These authors also observed that this loss in intensity could not be recovered when the potential was returned to its initial value (1.00 V), which indicates that the material undergoes an irreversible process. Fig. 5 shows that a decrease in white line intensity was more pronounced for aut-IrO_x and this is possibly related to anion intercalation processes, as evidenced by the CV redox features observed over the 0.5–1.0 V range (Fig. 4).

The total surface areas of the electrocatalysts were evaluated by the Brunauer-Emmett-Teller (BET) method. All materials studied exhibit type-IV isotherms, characteristic of mesoporous materials (not shown here). The calculated BET surface areas of each catalyst is listed in Table 2, together with its pore volume (V_p) and total anodic CV charge (Q_{Total}), obtained by integrating the anodic CV curve (Fig. 4) and extrapolating to zero scan rate, as proposed in previous work [20,42].

Table 2 reveals that the BET surface area and pore volume decreases with increasing treatment temperature, which can be attributed to particle growth due to coalescence processes as observed by TEM (Fig. 2). The calculated BET surface area of the aut-IrO_x material is $141 \, m^2 \, g^{-1}$, while that for the IrO_2 – 500 °C catalyst is only $10 \, m^2 \, g^{-1}$, which represents a decline in surface area of more than 90%.

The data in Table 2 show that the calculated Q_{Total} for IrO_x – 100 °C is lower by 30% when compared to that of the aut-IrO_x mate-
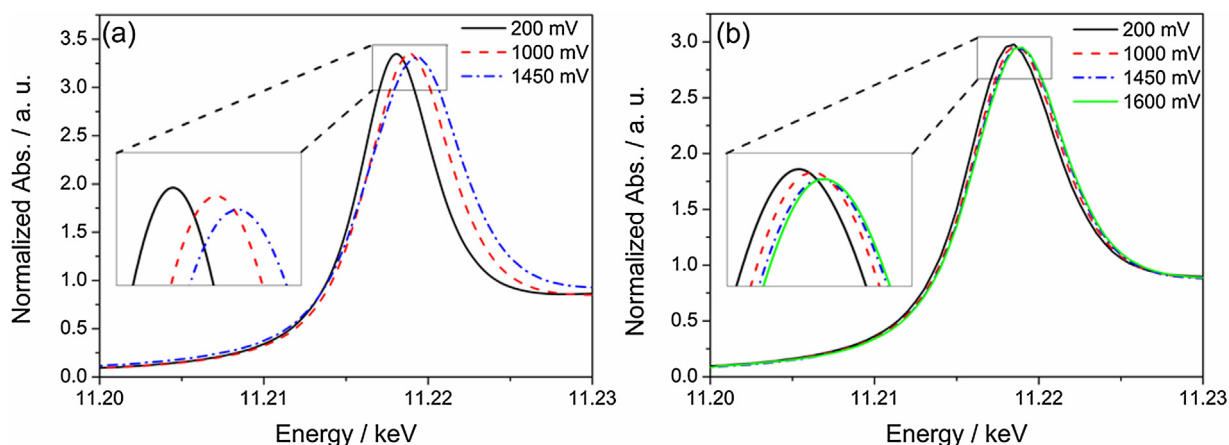
Fig. 5. Normalized XANES spectra at the Ir L3 edge for the (a) aut-IrO$_x$ and (b) IrO$_2$ – 500 °C electrocatalysts.

rial. This result is related to some extent to sample restructuring as a result of oxide dehydration, as evidenced by in the TGA results in Fig. S3.

However, after the temperature was raised to 200 and 300 °C, the calculated Q$_{Total}$ approaches that of aut-IrO$_x$, which may be due to changes in the composition of the material, in accordance with the differences in the CV profiles observed in Fig. 4. Such an effect could be related to an increase in the proportion of Ir^{+3} at the surface and/or sample dehydration, compared to the material produced at 100 °C (Table 1 and Fig. S3). After annealing at temperatures of 400 and 500 °C, the calculated Q$_{Total}$ values of the materials were 38 and 20 mC cm^{-2}, respectively, representing a fall of 60 and 80% in the electrochemical surface area compared to aut-IrO$_x$. These falls in surface areas are close to those determined using the BET method, and are consistent with increases in the crystallite/particle sizes discussed above. In contrast to what observed for the samples produced at 200 and 300 °C, the effect of increasing Ir^{+3} content in IrO$_2$ – 400 °C and IrO$_2$ – 500 °C materials is more than compensated for by large increases in particle size.

3.3. Activity and stability for the OER

The catalyst's activities towards the oxygen evolution reaction were evaluated through anodic polarization experiments. Fig. 6a displays potentiodynamic curves normalized by the geometric area of the glassy carbon substrate. The curves in Fig. 6a show that the OER current decreases with increasing annealing temperature. The Nyquist plots presented in Fig. S4 reveal that the high frequency intercepts are similar for both aut-IrO$_x$ and IrO$_2$ – 500 °C, which confirms that the ohmic resistance does not compromise a comparison between these catalysts during the polarization of the electrode for the OER. The reaction onset of the aut-IrO$_x$ material occurs at around 1.42 V and a current density of 35 mA cm^{-2} at 1.55 V, while for the material calcined at 500 °C the onset is close to 1.55 V and the current density at this potential is 5 mA cm^{-2}. In comparison, Markovic and co-workers reported an OER onset potential of 1.50 V, with a current density close to 2 mA cm^{-2} at 1.55 V, for a highly defective amorphous iridium oxide catalyst formed electrochemically from a well-characterized polycrystalline iridium [43]. Here, the higher catalytic mass-activities of materials calcined at low temperatures is attributed to the chemical nature of the iridium oxide [16]; hydrated amorphous iridium oxide is more active compared to non-hydrated crystalline IrO$_2$. Accordingly, defects, particle size, and oxide composition have been found to impact significantly on the performance of the catalyst. However, the preponderant effect of increased real surface area on improving activity cannot be disregarded.

Most of the charge involved in the low potential region, *i.e.*, below the OER onset in the i-E profiles of iridium oxides, can be considered to be capacitive and hence, proportional to the electrochemical surface area (ECSA). Therefore, the polarization curves can be normalized by the calculated total anodic charge (Q$_{Total}$) to obtaining the specific activity for each electrocatalysts. Here, because of changes in the surface compositions of the catalysts as functions of treatment temperature, particularly in the 100–200 °C range, there is some uncertainly in using this approach. However, the very good linear correlation between the values of Q$_{Total}$ and S, observed in the 200–500 °C range (Table 2 and Fig. S5) validate this procedure for calculating specific activities. Tafel plots of specific activities are shown in Fig. 6b. Curves for aut-IrO$_x$ and IrO$_x$ – 100 °C are included for consistency, although their morphologies and compositions differ more strongly from those of other catalysts.

Two Tafel linear regions can be distinguished in these plots, the first one corresponds to slopes close to 40 mV dec^{-1} in the low current density regions, and the second with slopes close to 120 mV dec^{-1} in the higher current density regions. Tafel slopes of 40 and 120 mV dec^{-1} have been reported for sputtered iridium oxide films [44], thermally prepared iridium oxides [16,45], and mixed oxides [46]. The normalized polarization curves depicted in Fig. 6b also reveal that the aut-IrO$_x$ material exhibits higher OER activity at lower current densities, while all heat-treated materials perform similarly. However, at higher current densities, the OER activity of the aut-IrO$_x$ material is comparable to those of the electrocatalysts heated to 300 °C, whereas the IrO$_2$ – 400 °C and 500 °C materials have even higher specific activities.

The specific activity is a very important piece of information that indicates how well the activity/stability of a catalyst has been tuned by thermal calcination and, as will be seen later, IrO$_2$ – 400 °C and IrO$_2$ – 500 °C present better balances between specific activity and stability over the OER potential range. Iridium oxide calcined at 400/500 °C was also reported to perform better when applied in a solid polymer electrolyzer [47]. An important challenge for future investigations is the production of these same materials with high porosities and/or smaller particle sizes in order to enhance the specific surface areas, as has been attempted for other iridium oxide films by a templating procedure [33].

The OER mechanism for catalysis by the IrO$_x$ materials prepared in this work can be based on theoretical studies reported by Rossmeisl et al. [48] on the thermochemistry of elementary steps in the oxidation of water on RuO$_2$ and IrO$_2$. Accordingly, oxygen evolution comprises four steps that involve three oxygen-adsorbed species (OH$_{ad}$, O$_{ad}$ and OOH$_{ad}$) plus the active site (IrO$_x$, denoted by *) as
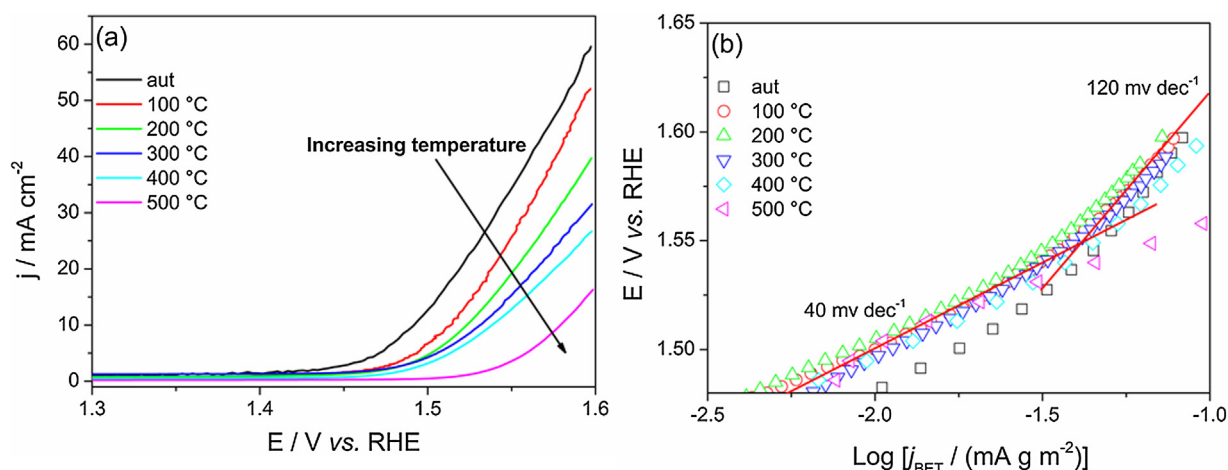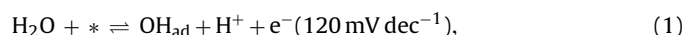
Fig. 6. (a) OER polarization curves at 5 mV s^{-1} and 1600 rpm. The currents have been normalized by the glassy carbon substrate area. (b) Corresponding Tafel diagrams of the studied IrO$_x$ catalysts.

intermediates in the overall process, as shown in equations (1) to (4):

$$H_2O + * \rightleftharpoons OH_{ad} + H^+ + e^- (120\, mV\, dec^{-1}), \qquad (1)$$

$$OH_{ad} \rightleftharpoons O_{ad} + H^+ + e^- (40\, mV\, dec^{-1}), \qquad (2)$$

$$O_{ad} + H_2O \rightleftharpoons OOH_{ad} + H^+ + e^-, \qquad (3)$$

with oxygen evolution finally taking place through:

$$OOH_{ad} \rightleftharpoons * + O_2 + H^+ + e^- \qquad (4)$$

where the numbers in parentheses are the Tafel slopes calculated by considering the different reactions as rate determining steps [45].

The Tafel slopes calculated from Fig. 6b are in good agreement with the predicted slopes and suggest that at low current densities deprotonation of the adsorbent (Eq. (2)) is the rate limiting step in the OER process. At higher current densities, the slopes are 120 mV dec^{-1}, indicating that the rate determining step moves to the oxidative adsorption of water (Eq. (1)).

Metallic iridium is known for its elevated resistance to corrosion and even iridium oxide is usually chosen as an OER catalyst because of its higher stability compared to other highly active materials such as Ru and RuO$_2$. Here, the stabilities of the IrO$_x$ catalysts were examined using two protocols, as described in part 2.3 (above). Fig. 7a and b displays the CV profiles of the aut-IrO$_x$ and IrO$_2$–500 °C catalysts after 1000 (one thousand) potential cycles between 0.3 and 1.2 V at 50 mV s^{-1} in 0.5 M H$_2$SO$_4$. The corresponding profiles for the other IrO$_x$ electrocatalysts after 1000 cycles can be found in Fig. S6. No CV-profile changes were observed for any catalyst after 1000 potential cycles, revealing that all oxides are stable under these aging conditions. Audichon et al. evaluated the stabilities of RuO$_2$, IrO$_2$, and IrO$_2$@RuO$_2$ obtained at 400 °C using the same protocol [21]; the shapes of the CV profiles of these three catalysts did not change after 1000 potential cycles either, which is similar to that observed in Fig. 7.

We note that the aging protocol described above may not provide assurance that the catalysts are stable over course of the OER, since the onset potential for this reaction is higher than the upper limit of the potentials in Fig. 7 and Fig. S6, as shown in Fig. 6. To evaluate the stabilities of the synthesized IrO$_x$ catalysts in the OER region, a protocol involving 500 potential cycles between 1.1 and 1.6 V at 50 mV s^{-1} was used, and the OER activities were reevaluated after every 100 cycles. The results for the aut-IrO$_x$ and IrO$_2$ – 500 °C materials are shown in Fig. 8, with the results for the other materials available in Fig. S7. For comparison, Fig. 8c shows plots

Table 3
Iridium mass compositions obtained by EDX analyses of the catalytic layers before and after 500 aging cycles (1.1–1.6 V at 50 mV s^{-1}).

IrO$_x$	Ir mass (%)	
	Before	After
aut	80	65
100 °C	80	73
200 °C	84	80
300 °C	85	82
400 °C	83	82
500 °C	87	88

of current densities at the constant electrode potential of 1.55 V, as functions of time for all catalysts. In this instance, the current densities are expressed per unit of geometric area.

As shown in Fig. 8a and b, both catalysts display sharp decreases in activity over the first 100 cycles. Decreases in OER currents are also observed for the others catalysts (Fig. S7), which is probably attributable to the accumulation of oxygen bubbles in the catalyst's pores [49]. According to the Nyquist diagram (Fig. S4), the aut-IrO$_x$ material does not exhibit any difference in resistance in the higher frequency region before and after 100 CV cycles. Over the next 400 cycles, a progressive decline in activity is seen for each material (Fig. 8a,b and S7), but in the case of IrO$_2$ – 500 °C there is a tendency toward stabilization after a total of 400 cycles (Fig. 8b). In agreement with these results, chronoamperometric curves obtained at 1.55 V (Fig. 8c) provide evidence that the aut-IrO$_x$ material shows the largest drop in activity over the studied time period. However, despite this loss in the performance, the aut-IrO$_x$ material remains as the most active catalyst for OER during the stability experiments (Fig. 8a,c) followed by IrO$_x$ – 100 °C (Fig. S7).

As previously reported for different IrO$_2$ films [17,43], the greater stabilities of IrO$_2$ – 400 °C and 500 °C compared to aut-IrO$_x$ are related to higher degrees of crystallinity and surface oxygen content, as confirmed by XRD and XPS (Fig. 1 and Fig. S2, respectively). To further investigate iridium dissolution, iridium content was determined directly from each catalytic layer, before and after 500 cycles, using the EDX technique; the results of which are presented in Table 3. The EDX data show that the relative percentages of iridium decrease for aut-IrO$_x$ and IrO$_2$ – 100 °C after several cycles. The relative iridium content remained constant for remaining catalysts, suggesting that processes other than iridium dissolution, such as water absorption/adsorption from the electrolyte solution, occur during catalyst cycling, particularly for aut-IrO$_x$ and IrO$_x$ – 100 °C.
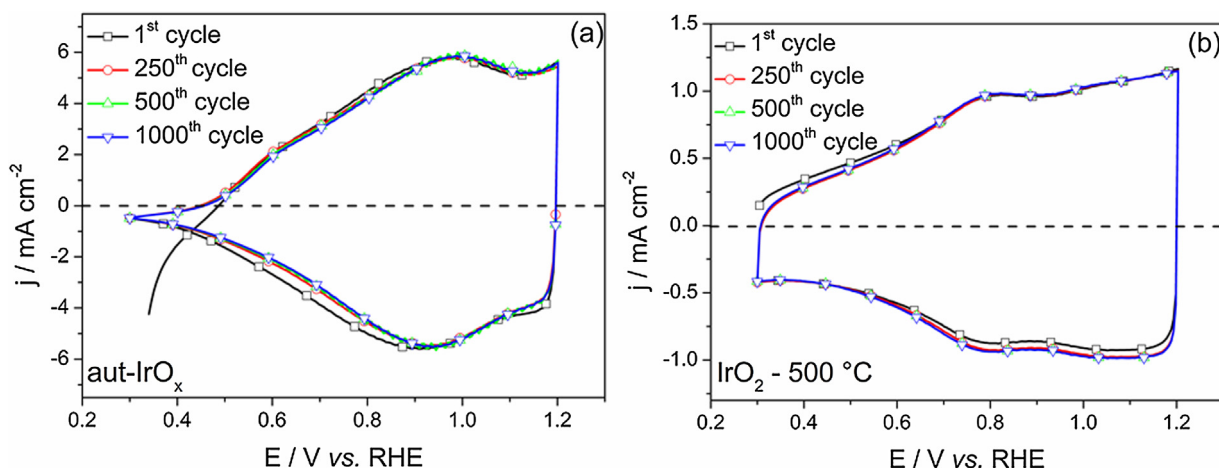
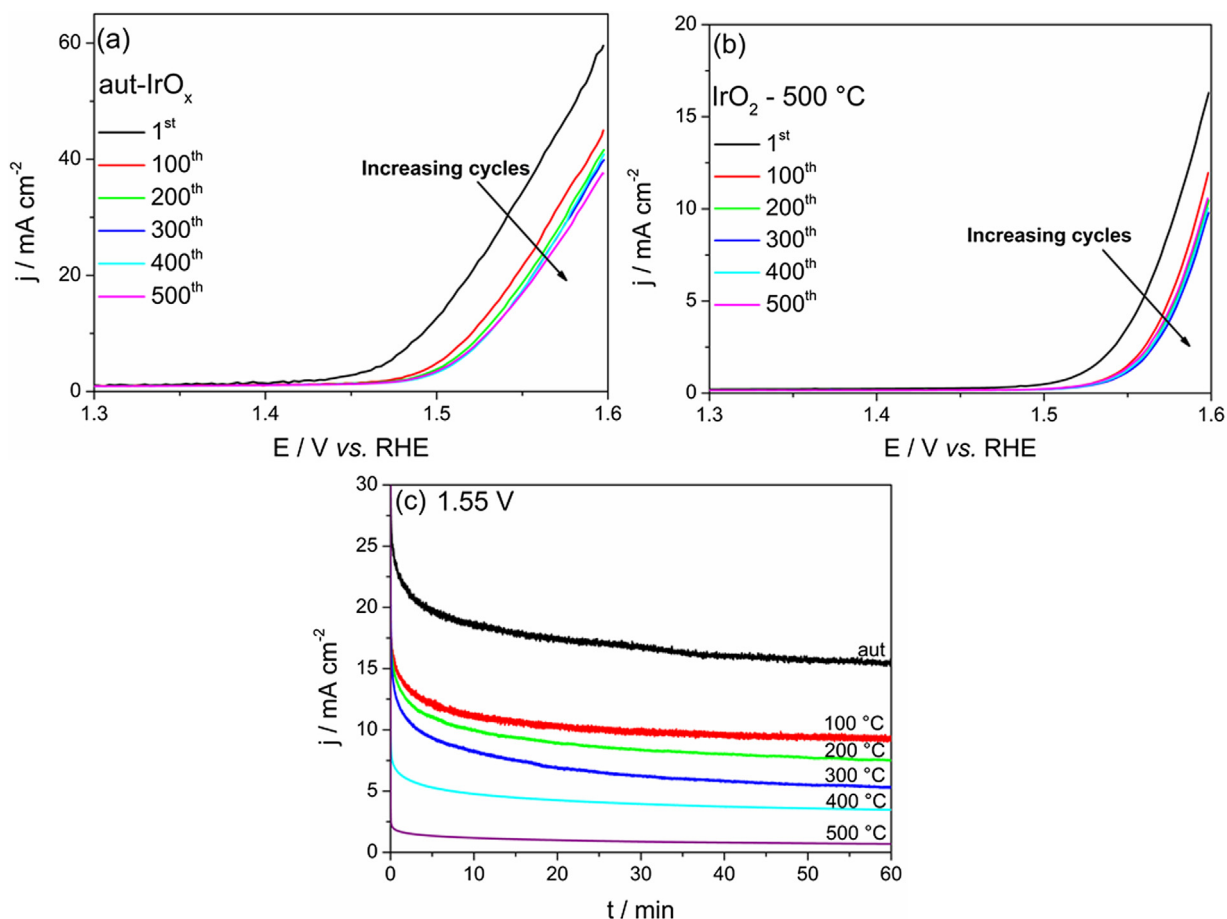Fig. 7. Cyclic voltammograms after 1000 aging cycles for (a) aut-IrO$_x$ and (b) IrO$_2$ – 500 °C.

Fig. 8. OER polarization curves (5 mV s^{-1}, 1600 rpm) after every hundred aging cycles for the (a) aut-IrO$_x$ and (b) IrO$_2$ – 500 °C catalysts in 0.5 M H$_2$SO$_4$ at 25 °C. (c) Chronoamperometric curves recorded at 1.55 V for the IrO$_x$ catalysts.

Electrode degradation processes were investigated using the identical location transmission electron microscopy (ILTEM) technique. The results for the aut-IrO$_x$ and IrO$_2$–500 °C, the least and most stable materials, respectively, are shown in Figs. 9 and 10. Fig. 9 and Fig. S8 reveal that the main processes responsible for the degradation in the activity of the aut-IrO$_x$ catalyst is the general shrinkage of the overall particle agglomeration spot due to the re-accommodation of particles, catalyst corrosion, particle clumping, or detachment and material coalescence, which have

also been observed for Pt-based catalyst used in PEMFCs [50–52]. On the other hand, the ILTEM micrographs of the IrO$_2$ – 500 °C catalyst (Fig. 10a and b) shows no evidence of any significant differences in the chosen regions before and after the electrochemical experiments, indicating that this material is much more stable than aut-IrO$_x$, maintaining its initial characteristics over the 500 aging cycles. In the micrographs depicted in Fig. 10d, some particle detachment is evident (blue circle). However, since one of the particles indicated by the blue circle is very small,
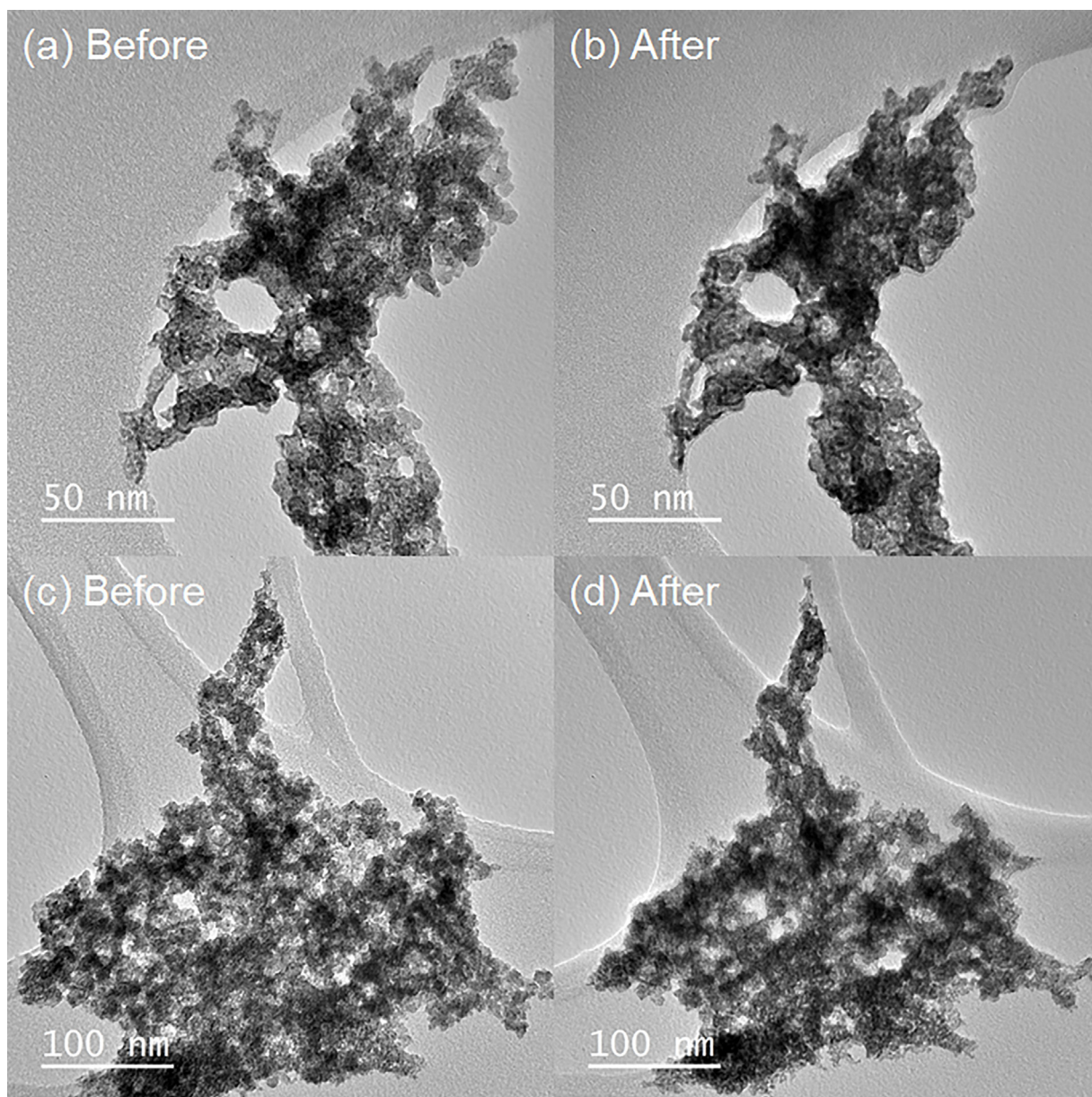
Fig. 9. ILTEM micrographs of two regions of the aut-IrO$_x$ catalyst before (a and c) and after (b and d) 500 potential aging cycles (1.1–1.6 V, 50 mV s^{-1}) in 0.5 M H$_2$SO$_4$ at 25 °C.

the possibility of chemical corrosion/redeposition cannot be ruled out.

4. Conclusions

The structures, activities and stabilities of hydrothermally prepared iridium oxide nanoparticles as catalysts for the OER were studied. Heat treatment at different temperatures provided IrO$_x$ catalysts with varying degrees of crystallinity. EDX results confirm that these materials are composed mainly of iridium and oxygen, while XPS data reveal the existence of both Ir^{3+} and Ir^{4+} species on the surfaces of the catalysts. However, *in-situ* XAS analysis of the IrO$_2$ – 500 °C material show that the bulk of the catalyst is more oxidized compared to the aut-IrO$_x$ material.

Voltammetric analyses show that materials calcined at lower temperatures have characteristic CV profiles of hydrous amorphous iridium, while for the IrO$_2$ – 400 °C and 500 °C samples, the CV profiles are similar to that of thermally prepared iridium oxide. Oxygen evolution reaction polarization curves reveal that the catalysts'

activities decrease with increasing calcination temperature; however, at higher current densities, the OER activity of the aut-IrO$_x$ material becomes comparable to those of the electrocatalysts prepared by heating to temperatures up to, but below 300 °C, whereas the IrO$_2$ – 400 °C and 500 °C catalysts exhibit even higher specific activities.

Aging experiments show that catalyst degradation begins as the OER begins. Results after 500 potential cycles between 1.1 and 1.6 V reveal that the catalysts calcined at higher temperatures are more stable. EDX analyses performed directly on the catalytic layers show that the catalysts produced at lower temperature had lost of iridium during the aging experiments. Nonetheless, ILTEM analyses reveal that iridium dissolution is not the only degradation process responsible for the instabilities of these materials; particles detachment and clumping also play roles.

Finally, we showed that the IrO$_2$ – 400 °C and IrO$_2$ – 500 °C exhibit better balances between specific activity and stability over the potential range of the OER. The higher stabilities of both the IrO$_2$ – 400 °C and IrO$_2$ – 500 °C catalysts are attributed to their increased
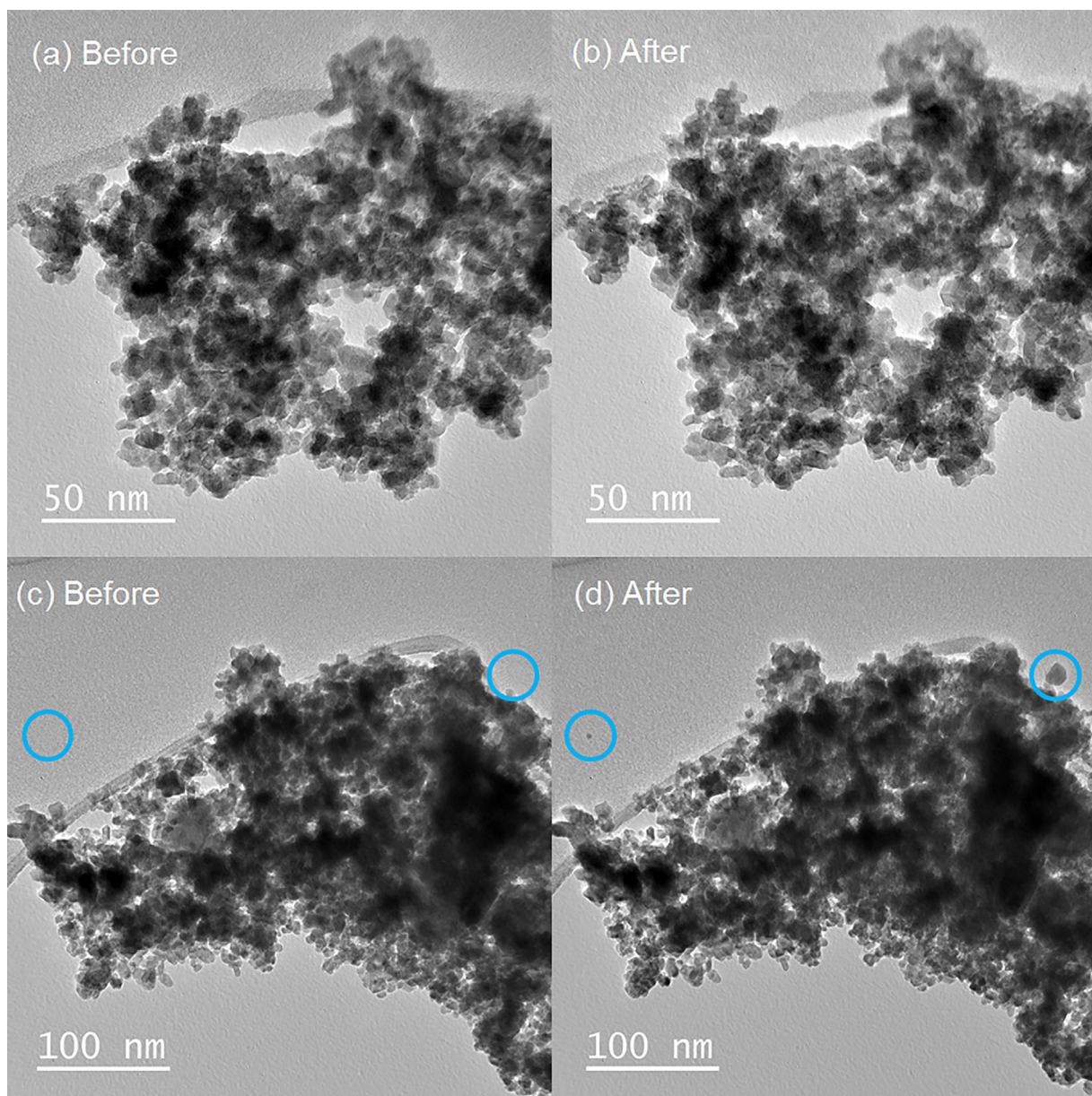
Fig. 10. ILTEM micrographs of two regions of the $IrO_2-500\,°C$ catalyst before (a and c) and after (b and d) 500 potential aging cycles (1.1–1.6 V, 50 mV s^{-1}) in 0.5 M H_2SO_4 at 25 °C.

crystallinities and surface oxygen contents, as confirmed XRD and XPS. The high initial performance loss of the aut-IrO$_x$ material is related to its amorphous structure. However, despite its lower stability, this catalyst still shows the higher mass activity at the end of the aging experiments, which should be considered during the development of iridium-oxide-based catalysts for use in oxygen evolution reaction.

Appendix A. Supplementary data

Supplementary data associated with this article can be found, in the online version, at **http://dx.doi.org/10.1016/j.apcatb.2017.06.044**.

References

[1] P. Tseng, J. Lee, P. Friley, Energy 30 (2005) 2703–2720.
[2] M. Ball, M. Wietschel, Int. J. Hydrogen Energy 34 (2009) 615–627.
[3] M. Carmo, D.L. Fritz, J. Mergel, D. Stolten, Int. J. Hydrogen Energy 38 (2013) 4901–4934.
[4] A.S. Aricò, S. Siracusano, N. Briguglio, V. Baglio, A. Di Blasi, V. Antonucci, J. Appl. Electrochem. 43 (2013) 107–118.
[5] J.K. Nørskov, T. Bligaard, A. Logadottir, J.R. Kitchin, J.G. Chen, S. Pandelov, U. Stimming, J. Electrochem. Soc. 152 (2005) J23–J26.
[6] W. Sheng, H.A. Gasteiger, Y. Shao-Horn, J. Electrochem. Soc. 157 (2010) B1529–B1536.
[7] H. Dau, C. Limberg, T. Reier, M. Risch, S. Roggan, P. Strasser, ChemCatChem 2 (2010) 724–761.

[8] I.C. Man, H.Y. Su, F. Calle-Vallejo, H.A. Hansen, J.I. Martínez, N.G. Inoglu, J. Kitchin, T.F. Jaramillo, J.K. Nørskov, J. Rossmeisl, ChemCatChem 3 (2011) 1159–1165.

[9] S. Cherevko, S. Geiger, O. Kasian, N. Kulyk, J.-P. Grote, A. Savan, B.R. Shrestha, S. Merzlikin, B. Breitbach, A. Ludwig, Catal. Today 262 (2016) 170–180.

[10] E. Antolini, ACS Catal. 4 (2014) 1426–1440.

[11] T. Reier, M. Oezaslan, P. Strasser, Acs Catal. 2 (2012) 1765–1772.

[12] S. Song, H. Zhang, X. Ma, Z. Shao, R.T. Baker, B. Yi, Int. J. Hydrogen Energy 33 (2008) 4955–4961.

[13] R. Kötz, S. Stucki, Electrochim. Acta 31 (1986) 1311–1316.

[14] J. Cheng, H. Zhang, G. Chen, Y. Zhang, Electrochim. Acta 54 (2009) 6250–6256.

[15] L. Ouattara, S. Fierro, O. Frey, M. Koudelka, C. Comninellis, J. Appl. Electrochem. 39 (2009) 1361–1367.

[16] T. Reier, I. Weidinger, P. Hildebrandt, R. Kraehnert, P. Strasser, ECS Trans. 58 (2013) 39–51.

[17] S. Cherevko, T. Reier, A.R. Zeradjanin, Z. Pawolek, P. Strasser, K.J. Mayrhofer, Electrochem. Commun. 48 (2014) 81–85.

[18] N. Bestaoui, E. Prouzet, Chem. Mater. 9 (1997) 1036–1041.

[19] B. Ravel, M. Newville, J. Synchrotron Radiat. 12 (2005) 537–541.

[20] S. Ardizzone, G. Fregonara, S. Trasatti, Electrochim. Acta 35 (1990) 263–267.

[21] T. Audichon, T.W. Napporn, C. Canaff, C.U. Morais, C.M. Comminges, K.B. Kokoh, J. Phys. Chem. C 120 (2016) 2562–2573.

[22] Y. Lee, J. Suntivich, K.J. May, E.E. Perry, Y. Shao-Horn, J. Phys. Chem. Lett. 3 (2012) 399–404.

[23] A. Talanov, W.A. Phelan, Z.A. Kelly, M.A. Siegler, T.M. McQueen, Inorg. Chem. 53 (2014) 4500–4507.

[24] W. Sun, Y. Song, X.-Q. Gong, L.-m. Cao, J. Yang, ACS Appl. Mater. Interfaces 8 (2016) 820–826.

[25] H. Rietveld, J. Appl. Crystallogr. 2 (1969) 65–71.

[26] L. Atanasoska, R. Atanasoski, S. Trasatti, Vacuum 40 (1990) 91–94.

[27] S. Anantharaj, P. Karthik, S. Kundu, J. Mater. Chem. A 3 (2015) 24463–24478.

[28] Y.Q. Shao, Z.Y. Yi, C. He, J.Q. Zhu, D. Tang, J. Am. Ceram. Soc. 98 (2015) 1485–1492.

[29] M. Peuckert, Surf. Sci. 144 (1984) 451–464.

[30] R. Sanjines, A. Aruchamy, F. Levy, J. Electrochem. Soc. 136 (1989) 1740–1743.

[31] B.E. Conway, J. Mozota, Electrochim. Acta 28 (1983) 9–16.

[32] S. Gottesfeld, S. Srinivasan, J. Electroanal. Chem. Interfacial Electrochem. 86 (1978) 89–104.

[33] M. Bernicke, E. Ortel, T. Reier, A. Bergmann, J. Ferreira de Araujo, P. Strasser, R. Kraehnert, ChemSusChem 8 (2015) 1908–1915.

[34] A. Minguzzi, C. Locatelli, O. Lugaresi, E. Achilli, G. Cappelletti, M. Scavini, M. Coduri, P. Masala, B. Sacchi, A. Vertova, ACS Catal. 5 (2015) 5104–5115.

[35] J.-H. Choy, D.-K. Kim, G. Demazeau, D.-Y. Jung, J. Phys. Chem. 98 (1994) 6258–6262.

[36] D.F. Abbott, D. Lebedev, K. Waltar, M. Povia, M. Nachtegaal, E. Fabbri, C. Copéret, T.J. Schmidt, Chem. Mater. 28 (2016) 6591–6604.

[37] A. Shukla, R. Raman, N. Choudhury, K. Priolkar, P. Sarode, S. Emura, R. Kumashiro, J. Electroanal. Chem. 563 (2004) 181–190.

[38] J. McBreen, S. Mukerjee, J. Electrochem. Soc. 142 (1995) 3399–3404.

[39] S. Mukerjee, J. McBreen, J. Electroanal. Chem. 448 (1998) 163–171.

[40] S. Mukerjee, S. Srinivasan, M.P. Soriaga, J. McBreen, J. Phys. Chem. 99 (1995) 4577–4589.

[41] A.R. Hillman, M.A. Skopek, S.J. Gurman, PCCP 13 (2011) 5252–5263.

[42] C. Rozain, E. Mayousse, N. Guillet, P. Millet, Appl. Catal. B 182 (2016) 153–160.

[43] N. Danilovic, R. Subbaraman, K.-C. Chang, S.H. Chang, Y.J. Kang, J. Snyder, A.P. Paulikas, D. Strmcnik, Y.-T. Kim, D. Myers, J. Phys. Chem. Lett. 5 (2014) 2474–2478.

[44] E. Slavcheva, I. Radev, S. Bliznakov, G. Topalov, P. Andreev, E. Budevski, Electrochim. Acta 52 (2007) 3889–3894.

[45] S. Fierro, A. Kapałka, C. Comninellis, Electrochem. Commun. 12 (2010) 172–174.

[46] R. Tunold, A.T. Marshall, E. Rasten, M. Tsypkin, L.-E. Owe, S. Sunde, ECS Trans. 25 (2010) 103–117.

[47] J.C. Cruz, V. Baglio, S. Siracusano, R. Ornelas, L. Ortiz-Frade, L.G. Arriaga, V. Antonucci, A.S. Aricò, J. Nanopart. Res. 13 (2011) 1639–1646.

[48] J. Rossmeisl, Z.W. Qu, H. Zhu, G.J. Kroes, J.K. Nørskov, J. Electroanal. Chem. 607 (2007) 83–89.

[49] Y. Liang, Y. Li, H. Wang, J. Zhou, J. Wang, T. Regier, H. Dai, Nat Mater 10 (2011) 780–786.

[50] L. Dubau, L. Castanheira, G. Berthomé, F. Maillard, Electrochim. Acta 110 (2013) 273–281.

[51] F.R. Nikkuni, E.A. Ticianelli, L. Dubau, M. Chatenet, Electrocatalysis 4 (2013) 104–116.

[52] F.J. Perez-Alonso, C.F. Elkjær, S.S. Shim, B.L. Abrams, I.E.L. Stephens, I. Chorkendorff, J. Power Sources 196 (2011) 6085–6091.